Heterogeneous lamella structure unites ultrafine-grain strength with coarse-grain ductility

Xiaolei Wu[a,1], Muxin Yang[a], Fuping Yuan[a], Guilin Wu[b], Yujie Wei[a], Xiaoxu Huang[b], and Yuntian Zhu[c,d,1]

[a]State Key Laboratory of Nonlinear Mechanics, Institute of Mechanics, Chinese Academy of Sciences, Beijing 100190, China; [b]College of Materials Science and Engineering, Chongqing University, Chongqing 400044, China; [c]School of Materials Science and Engineering, Nanjing University of Science and Technology, Nanjing 210094, China; and [d]Department of Materials Science and Engineering, North Carolina State University, Raleigh, NC 27695

Edited by David A. Weitz, Harvard University, Cambridge, MA, and approved October 21, 2015 (received for review August 28, 2015)

Grain refinement can make conventional metals several times stronger, but this comes at dramatic loss of ductility. Here we report a heterogeneous lamella structure in Ti produced by asymmetric rolling and partial recrystallization that can produce an unprecedented property combination: as strong as ultrafine-grained metal and at the same time as ductile as conventional coarse-grained metal. It also has higher strain hardening than coarse-grained Ti, which was hitherto believed impossible. The heterogeneous lamella structure is characterized with soft micrograined lamellae embedded in hard ultrafine-grained lamella matrix. The unusual high strength is obtained with the assistance of high back stress developed from heterogeneous yielding, whereas the high ductility is attributed to back-stress hardening and dislocation hardening. The process discovered here is amenable to large-scale industrial production at low cost, and might be applicable to other metal systems.

back-stress hardening | heterogeneous lamella structure | ductility | strength | strain partitioning

Strong or ductile? For centuries engineers have been forced to choose one of them, not both as they would like to. This is because a material is either strong or ductile but rarely both at the same time. High strength is always desirable, especially under the current challenge of energy crisis and global warming, where stronger materials can help by making transportation vehicles lighter to improve their energy efficiency. However, good ductility is also required to prevent catastrophic failure during service.

Grain refinement has been extensively explored to strengthen metals. Ultrafine-grained (UFG) and nanostructured metals can be many times stronger than their conventional coarse-grained (CG) counterparts (1–5), but low ductility is a roadblock to their practical applications. The low ductility is primarily due to their low strain hardening (6–12), which is caused by their small grain sizes. To further exacerbate the problem, their high strengths require UFG metals to have even higher strain hardening than weaker CG metals to maintain the same ductility according to the Considère criterion. This makes it appear hopeless for UFG materials to have high ductility and it has been taken for granted that they are super strong but inevitably much less ductile than their CG counterparts.

Microstructure of Heterogeneous Lamella Structure

Here we report that a previously unidentified heterogeneous lamella (HL) structure possesses both the UFG strength and the CG ductility, which to our knowledge has never been realized before. The HL structure was produced by asymmetric rolling (13, 14) and subsequent partial recrystallization (see *Materials and Methods* for details). The asymmetric rolling elongated the initial equiaxed grains (Fig. 1*A*) into a lamella structure (Fig. 1*B*), which is heterogeneous with some areas having finer lamella spacing than others. This was due to the variation of slip systems and plastic strain in grains with different initial orientation (15). The asymmetric rolling also imparts a higher strain near the sample surface (14), which produces a nanostructured surface layer (Fig. 1*C*) as well as a slight structure gradient before and after recrystallization. During the subsequent partial recrystallization, the lamellae with finer structure recrystallized to form soft microcrystalline lamellae while others underwent recovery to maintain the hard UFG structure (15) (Fig. 1*D*). Fig. 1*E* shows the distribution of recrystallized grains (RGs) with sizes larger than 1 μm after blacking out UFG areas. Interestingly, most RGs cluster into long lamellae along the rolling direction, which are distributed within black UFG lamellae. Fig. 1*F* is a transmission electron microscopy (TEM) image showing a lamella of RGs between two UFG lamellae. The RGs are equiaxed and almost dislocation-free. In contrast, the smaller UFG grains still contain a high density of dislocations. Fig. 1*G* shows that the volume fraction of RGs decreases through the depth but their sizes increase slightly. The weak gradients in microstructure before and after recrystallization are reflected in the microhardness (Hv) variation in Fig. 1*H*. Tensile samples with different thickness were prepared by polishing away equal-thickness layers from both sides of the recrystallized sample (Fig. 1*H*).

Mechanical Properties and Strain Hardening of HL Structure

Fig. 2*A* and *B* shows that HL Ti, e.g., both HL60 and HL80 from the central 60-μm and 80-μm-thick layer, respectively, is as strong as UFG Ti and as ductile as CG Ti. The squares in Fig. 2*A* mark the start of necking according to the Considère criterion. Both HL60 and HL80 are three times as strong as CG Ti while maintaining the same ductility (the uniform tensile elongation) (Fig. 2*A*). Furthermore, all other HL Ti samples are also much stronger and more ductile than CG Ti (Fig. 2*B*). In contrast, the UFG Ti becomes mechanically unstable soon after yielding.

The HL Ti samples derive their high ductility from their high strain-hardening rate ($\Theta = d\sigma/d\varepsilon$), which becomes unprecedentedly higher than that of CG Ti after some plastic straining (Fig. 2*C*).

Significance

For centuries it has been a challenge to avoid strength–ductility trade-off, which is especially problematic for ultrastrong ultrafine-grained metals. Here we evade this trade-off dilemma by architecting a heterogeneous lamella structure, i.e., soft micrograined lamellae embedded in hard ultrafine-grained lamella matrix. The heterogeneous deformation of this previously unidentified structure produces significant back-stress hardening in addition to conventional dislocation hardening, rendering it higher strain hardening than coarse-grained metals. The high back-stress hardening makes the material as strong as ultrafine-grained metals and as ductile as coarse-grained metals.

Author contributions: X.W. designed research; X.W., M.Y., and G.W. performed research; M.Y., F.Y., G.W., Y.W., X.H., and Y.Z. analyzed data; and X.W. and Y.Z. wrote the paper.

The authors declare no conflict of interest.

This article is a PNAS Direct Submission.

Freely available online through the PNAS open access option.

[1]To whom correspondence may be addressed. Email: xlwu@imech.ac.cn or ytzhu@ncsu.edu.

This article contains supporting information online at www.pnas.org/lookup/suppl/doi:10.1073/pnas.1517193112/-/DCSupplemental.

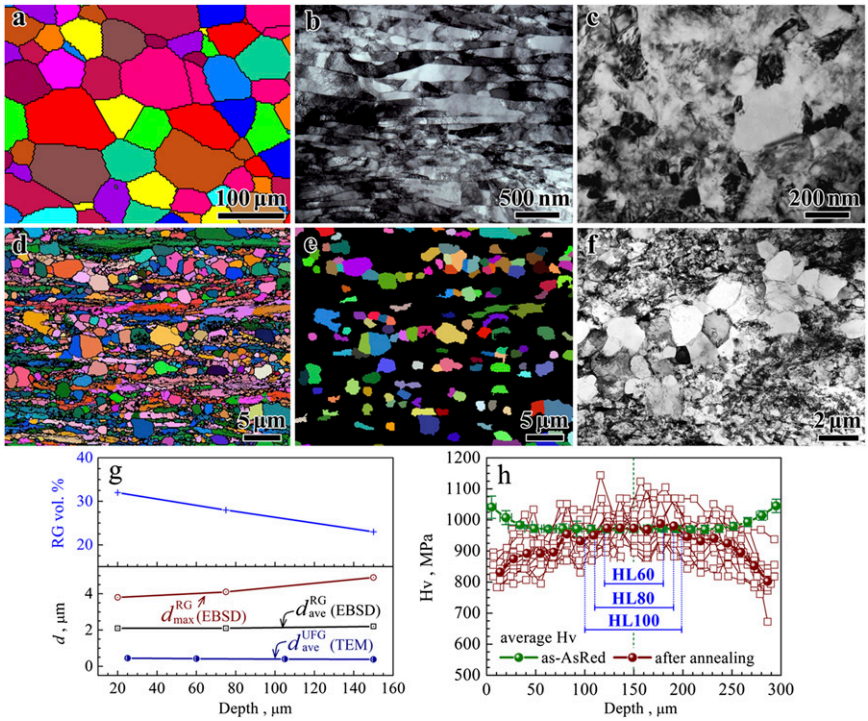

Fig. 1. Microstructure of HL Ti. (*A*) EBSD image of initial CG Ti. (*B* and *C*) TEM images showing nonuniform elongated lamellae in the central layer and nanograins in the top ∼25-μm surface layer after AsR. (*D*) EBSD image of HL Ti after partial recrystallization. (*E*) EBSD image of recrystallized grains (RGs) larger than 1 μm. (*F*) Cross-sectional TEM image of RG lamellae with two UFG lamellae on two sides. (*G*) Weak gradient distribution of RG volume fraction, RG average grain size (d^{RG}_{ave}), maximum size (d^{RG}_{max}), and mean grain size of UFG lamellae (d^{UFG}_{ave}) through the depth measured by EBSD and TEM. (*H*) Hv gradient in the as-rolled state and after partial recrystallization, together with the location of the tensile samples (e.g., HL60 means 60 μm in thickness). The large scattering in Hv data after partial recrystallization reflects the heterogeneous nature of HL Ti.

More remarkably, the HL60 sample has much higher strain hardening than the CG sample for the entire plastic deformation. Thicker HL Ti samples have a distinctive two-stage strain-hardening behavior, with initial low Θ, but higher Θ at larger plastic strains. Specifically, in stage I, Θ shows a steep drop at first followed by a steep upturn, typical of discontinuous yielding. This is due to the shortage of mobile dislocations at the onset of plastic deformation (8, 16), which makes it necessary for dislocations to glide faster to accommodate the applied constant strain rate. Higher stress is needed to move dislocations faster. Upon yielding, dislocations quickly multiply, leading to quick Θ increase due to dislocation interaction and entanglement. In stage II, Θ continues to rise, albeit at a relatively slow rate. This is surprising and, to our knowledge, has never been observed in either UFG or conventional CG metals, both of which have a typical monotonic drop in Θ.

Surprisingly, the weak Hv gradient disappeared after tensile testing (Fig. 2*D*), in contrast with what was observed in gradient structured steel (11). This indicates that the RGs were dramatically hardened by plastic deformation and the weak gradient in microstructure did not play a major role in mechanical properties. Note that Hv values are still scattered after tension, indicating that the heterogeneous mechanical properties remained after the tensile testing.

Bauschinger Effect and Back Stresses

The observed extraordinarily high strength of HL Ti can be attributed to its composite lamella nature. Under tensile loading, the soft lamellae of recrystallized micrograins will start plastic deformation first. However, they are constrained by surrounding hard lamellae so that dislocations in such grains are piled up and blocked at lamella interfaces, which are actually also grain boundaries. This produces a long-range back stress (17–19) to make it difficult for dislocations to slip in the micrograined lamellae until the surrounding UFG lamellae start to yield at a larger global strain. In other words, the internal back stress has significantly increased the flow stress of the soft lamellae by the time the whole sample is yielding. This is the primary reason for the observed high yield strength of HL Ti samples, as verified later by the back-stress calculation. This observation is consistent with the high strength caused by back stresses in passivated thin films (20–22) and nanopillars (23, 24).

To probe the origin of the high strain hardening of HL Ti and the contribution of back stress to the observed high yield strength, we conducted loading–unloading–reloading (LUR) testing (Fig. 3*A*) to investigate the Bauschinger effect, from which we can estimate the contributions of the back stress and dislocation hardening to the flow stress. Interestingly, HL Ti shows a very strong Bauschinger effect: during unloading, the reverse plastic flow (σ_{rev}) starts even when the applied stress is still in tension (Fig. 3*B*). A larger hysteresis loop during the unloading–reloading represents a stronger Bauschinger effect. As shown in Fig. 3*B*, the hysteresis loop becomes larger with increasing tensile strain for the HL Ti. Importantly, the hysteresis appeared even during the first unloading–reloading cycle near the yield point. In contrast, the CG Ti has negligible hysteresis (Fig. 3*B*). As schematically shown in Fig. 3*C*, the Bauschinger effect can be described by the reverse plastic strain (ε_{rp}) normalized by the yield strain (ε_y) (21, 24), which increases with increasing plastic strain (Fig. 3*D*). The back stress can be calculated as $\sigma_b = \sigma_f - \sigma_{eff}$ and $\sigma_{eff} = ((\sigma_f - \sigma_{rev})/2) + (\sigma*/2)$ (25), where σ_f denotes the flow stress, and σ_{eff}, σ_{rev}, and $\sigma*$ are defined in Fig. 3*C*.

As shown in Fig. 3*D*, the back stress is about 400 MPa near the yield point. The soft lamellae in HL Ti need to overcome this

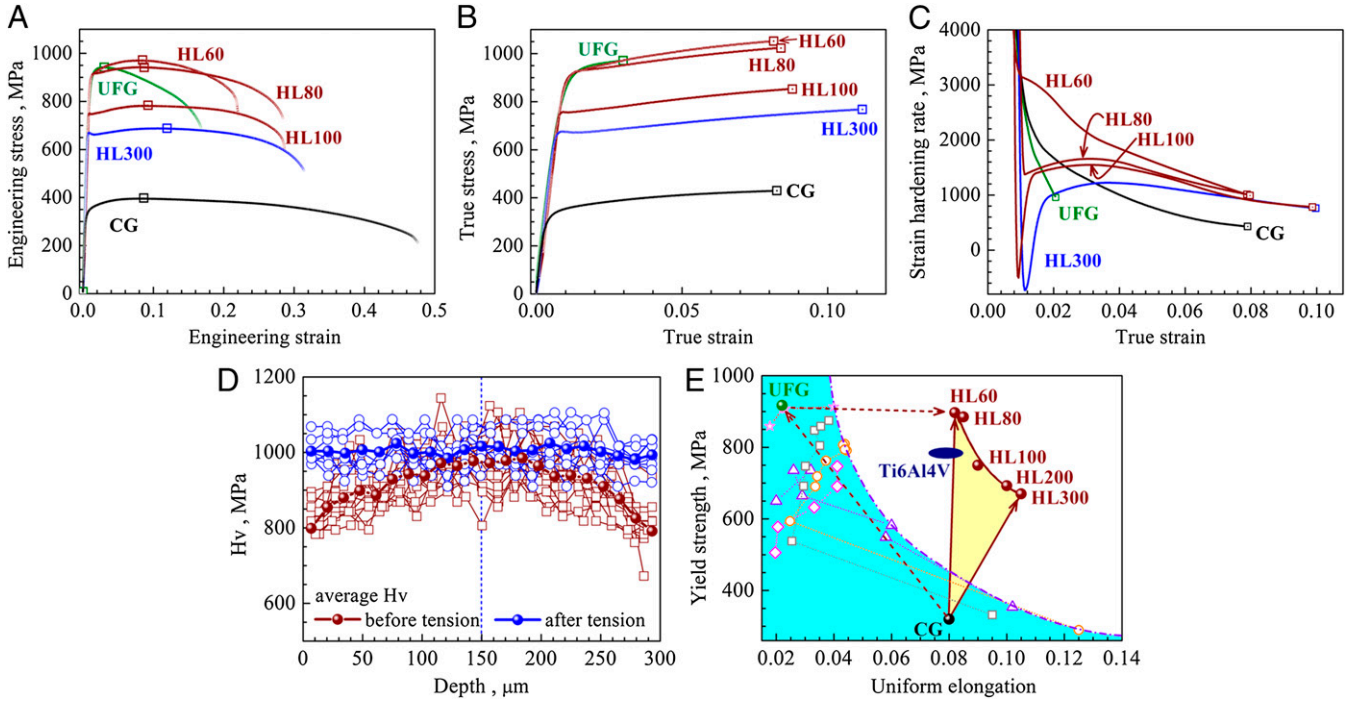

Fig. 2. Mechanical properties and strain hardening of HL Ti. (*A*) Tensile engineering stress–strain curves in HL Ti at a quasi-static strain rate of 5×10^{-4}·s^{-1} in comparison with UFG Ti and CG Ti. UFG sample: 300 μm thick as processed by AsR. HL Ti: annealed UFG at 475 °C for 5 min. The number after HL indicates the sample thickness (μm). The tensile samples were flat and dog-bone-shaped, with gauge dimension of 10 mm ×2.5 mm. (*B*) Tensile true stress–strain curves in HL Ti. (*C*) Strain hardening rate ($\Theta = d\sigma/d\varepsilon$) versus true strain of HL Ti. (*D*) Hv change before and after tensile testing at tensile strain of 10% in HL300. Solid points indicate the mean Hv values, whereas open indicate the experimentally measured values obtained by 10 time tests. Note the disappearance of a weak Hv gradient across the thickness after tensile testing. (*E*) Yield strength and uniform tensile elongation of HL Ti. Other data of Ti as well as Ti6Al4V are also shown for comparison.

additional high back stress to deform plastically, which contributes significantly to the observed high yield strength of the HL samples, especially the HL60 and HL80 samples. In other words, the observed high yield strength of HL samples resulted from the high back stress.

The back stress increased with plastic strain, especially at the early strain stage, which contributed to the high strain hardening. This is the primary reason why the strain hardening in HL Ti increased with applied global strain and surpassed that of CG-Ti, as shown in Fig. 2*C*. The homogeneous CG Ti does not show measurable Bauschinger effect or back stress, and its strain hardening decreased monotonically with the global strain. The effective stress, which includes the dislocation hardening and Peierls stress, is much lower than the back stress, which is consistent with an earlier report in constrained nanopillars (23). The increase in the effective stress with tensile strain should be primarily caused by dislocation density, i.e., dislocation hardening. Therefore, the high strain hardening originates from both back stress hardening and dislocation hardening. To the authors' best knowledge, the significant back-stress hardening has never been reported before.

The back-stress hardening is caused by the pile-up and accumulation of geometrically necessary dislocations. With increasing tensile strain, dislocation sources in the softer microcrystalline lamellae are activated first. However, the soft lamellae are surrounded and constrained by hard UFG lamellae, which are still deforming elastically. Therefore, dislocations in the soft lamellae cannot transmit into hard UFG lamellae. As shown in Fig. 4*A*, which is a TEM micrograph from an HL Ti sample tested at a tensile strain of 2%, dislocations piled up at several locations. All dislocations in an individual pile-up are from the same dislocation source and have the same Burgers vector. They consequently produce a long-range back stress to stop the dislocation source from emitting more dislocations. That is, soft lamellae constrained by hard lamella matrix appear much stronger than when they are not constrained. This explains why the HL60 and HL80 samples can be as strong as the UFG Ti, although they contain

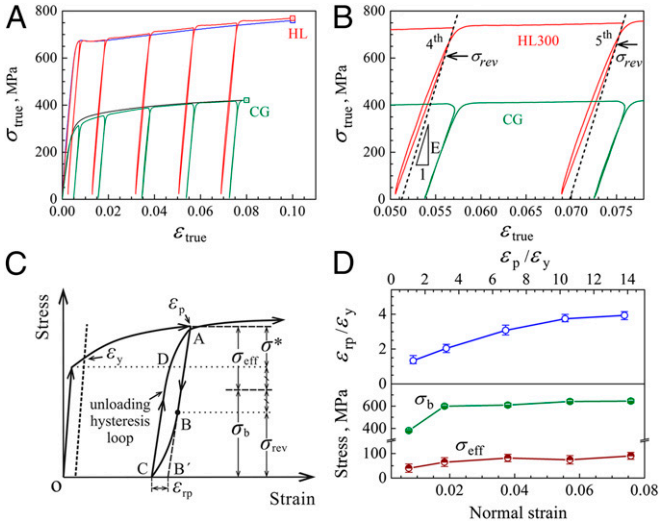

Fig. 3. Bauschinger effect and back stress of HL Ti. (*A*) LUR stress–strain curves of HL Ti and CG Ti. (*B*) Hysteresis loops. The two arrows indicate the reverse flow stress, i.e., σ_{rev}, deviating from the initial elastic behavior during unloading. (*C*) Schematic of calculating back stress (25). (*D*) Normalized reverse plastic strain, back stress, and effective stress versus applied strain.

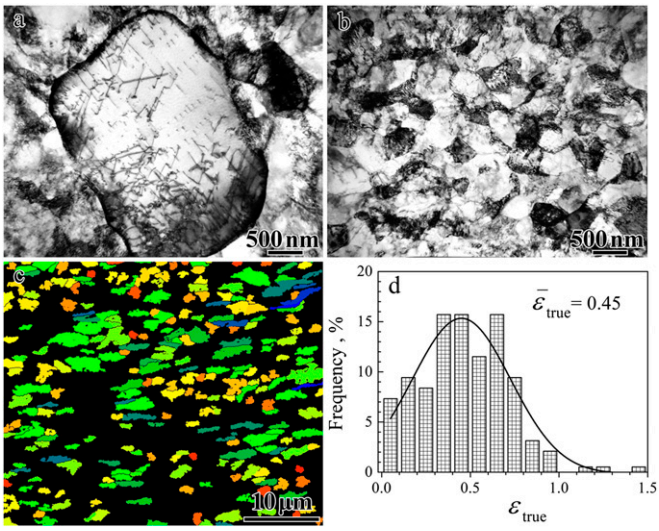

Fig. 4. Strain partitioning in HL Ti. (*A*) TEM image showing pile-up of dislocations in a recrystallized micrometer-sized grain at tensile strain of 2%. (*B*) TEM image showing equiaxed UFG in a sample tested to a tensile true strain of 9.4%. (*C*) EBSD image showing elongated RG along tensile direction at true strain of 9.5%. (*D*) Distribution of strains in RG with an average true strain of 0.45.

over 20% softer microcrystalline lamellae. It appears that the full constraint of the soft lamellae by the hard matrix is a prerequisite for this phenomenon.

Strain Partitioning

Beyond the yield point, the whole HL Ti sample is deformed plastically. However, the softer lamellae are easier to deform than hard lamellae. This causes plastic strain partitioning where the soft lamellae carry much higher plastic strain than hard lamellae. Indeed, after tensile testing for 9% true strain, the UFG in hard lamellae remain largely equiaxed (Fig. 4*B*), whereas most of the recrystallized micrometer-sized grains were deformed from equiaxed shape to elongated shape along the tensile direction (Fig. 4*C*). The true strain in each grain can be calculated from its aspect ratio α as $\varepsilon = (2/3)\ln \alpha$ (see the *Supporting Information*). After the HL Ti was deformed for a global true strain of 9.4%, the average true strain in recrystallized micrometer-sized grains was 45% (Fig. 4*D*). It should be noted that the real strain in the UFG lamella cannot be estimated using the grain geometry change because other deformation mechanisms such as coordinated deformation, grain boundary sliding, and grain rotation may also contribute to plastics strain when the grain sizes are very small (26). Nevertheless, the plastic strain in the hard UFG lamellae should be less than 9.4% because the soft lamellae carry much higher plastic strain of 45%. The strain has to be continuous at the interlamella interfaces, which further leads to strain gradient near these interfaces. Geometrically necessary dislocations (GNDs) will be generated to accommodate the strain gradient (27–29), which will generate long-range back stress near the interfaces. In other words, back-stress hardening in the HL Ti during plastic deformation is associated with strain partitioning, i.e., inhomogeneous plastic strain.

In addition to back stress, dislocation hardening, which is related to the increase in total dislocation density (29), should also contribute to the observed high strain hardening. The HL structure promotes the generation and accumulation of two types of the dislocations during the testing. One is the aforementioned GNDs, and the other is incidental type of dislocations that do not produce long-range back stress. It should be noted that local complex 3D stress states may develop from the applied uniaxial stresses due to the plastic incompatibility between the soft and hard lamellae. The stress state change will promote dislocation accumulation and interaction by activating more slip systems (11, 30, 31), similar to what occurs in gradient structures (11, 31). This will effectively increase the incidental dislocation density.

The HL structure can be considered as a special case of bimodal structure, but is much more effective in producing strain hardening than the reported conventional bimodal structure (6). Compared with the conventional bimodal structure, the HL structure possesses the following unique features that are essential for producing the observed extraordinary mechanical behavior: (*i*) the lamellar nature of the structure, (*ii*) the full constraint of the soft lamellae by harder matrix, and (*iii*) the high density of interlamella interfaces. First, it has been reported that the elongated inclusions produce higher strain hardening than spherical ones, especially when its long axis is aligned in the loading direction (32), which is the case in this study. The lamella geometry makes mutual constraint between the soft and hard lamellae more effective, which produces higher back stresses. Second, the full constraint of the soft lamellae by the hard lamella matrix makes it more effective to constrain the plastic deformation of the soft lamellae to develop higher back stresses than the conventional bimodal structure. Third, the HL structure has the high density of interlamella interfaces, where dislocation can pile up and accumulate to enhance back-stress hardening and dislocation hardening.

This work opens a new frontier toward high tensile ductility without sacrificing the high strength of UFG metals. Back stresses are primarily responsible for the observed high strength. Both back-stress hardening and dislocation hardening are responsible for the observed extraordinary strain-hardening rate and consequent high ductility. The lamella geometry, high constraint of the soft lamellae by hard matrix, and the high density of interfaces make it effective for developing back stress and dislocation hardening. The observations here provide a new principle for designing metals with mechanical properties that have not been reachable before. Importantly, the lamella structure is fabricated by asymmetric rolling followed by annealing, which is an industrial process that can be easily scaled up for large-scale production at low cost. The process discovered here might be applicable to other engineering metals and alloys, and needs further study.

Materials and Methods

Materials. Commercial pure titanium sheets 2.4 mm thick were used in the present study. The composition was (wt %) 0.10 C, 0.05 N, 0.015 H, 0.25 O, 0.30 Fe, bal. Ti. The sheets were vacuum-annealed at 700 °C for 2 h to achieve a fully homogeneous CG microstructure with a mean grain size of 43 μm.

HL-Structured Ti by Asymmetrical Rolling. Ti sheets 2.4 mm thick were processed by asymmetrical rolling (AsR) at room temperature. Rolling was conducted on a rolling mill with 45-mm-diameter rolls. The top and bottom rolls were driven at velocities of 1 m/s and 1.3 m/s, respectively, and a rolling reduction was 0.1 mm per pass. The Ti sheet was flipped over, and feeding direction was alternated from one end to the other between AsR passes. The sheets were finally rolled to 300 μm thick after 20 rolling passes with a total rolling reduction of 87.5%. No cracks were observed on the surface of the AsR-processed Ti sheets. The subsequent partial recrystallization was conducted in AsR-processed HL Ti sheets 300 μm thick at 475 °C for 5 min.

Tensile Test and LUR Test. All tensile specimens were dog-bone-shaped, with a gauge length of 10 mm and a width of 2.5 mm. To obtain reproducible tensile property, all tensile tests were repeated at least 3–5 times. The direction of tensile specimens was parallel to the rolling direction. Tensile samples, containing the central layer of various thicknesses, e.g., HL100, HL80, and HL60, etc. (number indicates the sample thickness, μm), was further obtained by taking off the equal thickness from two sides simultaneously in 300-μm-thick annealed HL samples.

Quasi-static uniaxial tensile tests were carried out using an Instron 5582 testing machine at strain rate of $5 \times 10^{-4}\cdot s^{-1}$ at room temperature. An extensometer was used to measure the strain during the tensile deformation. LUR tensile tests were conducted using an Instron 5966 testing machine at

room temperature. Five loading–unloading cycles were conducted during each tensile test. Upon straining to a designated strain (e.g., 2%) at strain rate of 5×10^{-4}·s^{-1}, the specimen was unloaded by the stress-control mode to 20 N at the unloading rate of 200 N·min^{-1}, followed by reloading at a strain rate of 5×10^{-4}·s^{-1} to the same applied stress before the next unloading.

Electron Back-Scattered Diffraction and TEM Observations. The cross-sectional and longitudinal electron back-scattered diffraction (EBSD) and TEM observations were conducted to investigate the microstructual evolution in HL Ti before and after tensile tests. TEM samples were cut from the gauge sections of tensile samples.

ACKNOWLEDGMENTS. The authors thank Prof. W. D. Nix for his insightful and constructive comments on this paper. X.W., M.Y., F.Y., and Y.W. are funded by the National Natural Science Foundation of China (11572328, 11072243, 11222224, 11472286, and 51471039) and Ministry of Science and Technology (2012CB932203, 2012CB937500, and 6138504). Y.Z. is funded by the US Army Research Office (W911 NF-12-1-0009), the US National Science Foundation (DMT-1104667), and the Nanjing University of Science and Technology.

1. Valiev RZ, Islamgaliev RK, Alexandrov IV (2000) Bulk nanostructured materials from severe plastic deformation. *Prog Mater Sci* 45(2):103–189.
2. Langdon TG (2013) Twenty-five years of ultrafine-grained materials: Achieving exceptional properties through grain refinement. *Acta Mater* 61(19):7035–7059.
3. Valiev RZ, Alexandrov IV, Zhu YT, Lowe TC (2002) Paradox of strength and ductility in metals processed by severe plastic deformation. *J Mater Res* 17(1):5–8.
4. Valiev RZ (2004) Nanostructuring of metals by severe plastic deformation for advanced properties. *Nat Mater* 3(8):511–516.
5. Zhu YT, Liao XZ (2004) Nanostructured metals: Retaining ductility. *Nat Mater* 3(6): 351–352.
6. Wang YM, Chen MW, Zhou FH, Ma E (2002) High tensile ductility in a nanostructured metal. *Nature* 419(6910):912–915.
7. Lu L, Shen YF, Chen XH, Qian LH, Lu K (2004) Ultrahigh strength and high electrical conductivity in copper. *Science* 304(5669):422–426.
8. Huang XX, Hansen N, Tsuji N (2006) Hardening by annealing and softening by deformation in nanostructured metals. *Science* 312(5771):249–251.
9. Fang TH, Li WL, Tao NR, Lu K (2011) Revealing extraordinary intrinsic tensile plasticity in gradient nano-grained copper. *Science* 331(6024):1587–1590.
10. Wei YJ, et al. (2014) Evading the strength-ductility trade-off dilemma in steel through gradient hierarchical nanotwins. *Nat Commun* 5:3580.
11. Wu XL, Jiang P, Chen L, Yuan FP, Zhu YT (2014) Extraordinary strain hardening by gradient structure. *Proc Natl Acad Sci USA* 111(20):7197–7201.
12. Wu XL, et al. (2015) Nanodomained nickel unite nanocrystal strength with coarse-grain ductility. *Sci Rep* 5:11728.
13. Roumina R, Sinclair CW (2008) Deformation geometry and through-thickness strain gradients in asymmetric rolling. *Metall Mater Trans A* 39(10):2495–2503.
14. Yu HL, et al. (2012) Asymmetric cryorolling for fabrication of nanostructural aluminum sheets. *Sci Rep* 2:772.
15. Wu G, Jensen DJ (2005) Recrystallisation kinetics of aluminium AA1200 cold rolled to true strain of 2. *Mater Sci Technol* 21(12):1407–1411.
16. Uchic MD, Dimiduk DM, Florando JN, Nix WD (2004) Sample dimensions influence strength and crystal plasticity. *Science* 305(5686):986–989.
17. Gibeling JC, Nix WD (1980) A numerical study of long range internal stresses associated with subgrain boundaries. *Acta Metall* 28(12):1743–1752.
18. Mughrabi H (1983) Dislocation wall and cell structures and long-range internal stresses in deformed metal crystals. *Acta Metall* 31(9):1367–1379.
19. Sinclair CW, Saada G, Embury JD (2006) Role of internal stresses in co-deformed two-phase materials. *Philos Mag* 86(25-26):4081–4098.
20. Xiang Y, Vlassak JJ (2006) Bauschinger and size effects in thin-film plasticity. *Acta Mater* 54(20):5449–5460.
21. Xiang Y, Vlassak JJ (2005) Bauschinger effect in thin metal films. *Scr Mater* 53(2): 177–182.
22. Rajagopalan J, Han JH, Saif MTA (2008) Bauschinger effect in unpassivated freestanding nanoscale metal films. *Scr Mater* 59(7):734–737.
23. Jennings AT, et al. (2012) Higher compressive strengths and the Bauschinger effect in conformally passivated copper nanopillars. *Acta Mater* 60(8):3444–3455.
24. Lee SW, Jennings AT, Greer JR (2013) Emergence of enhanced strengths and Bauschinger effect in conformally passivated copper nanopillars as revealed by dislocation dynamics. *Acta Mater* 61(6):1872–1885.
25. Feaugas X (1999) On the origin of the tensile flow stress in the stainless steel AISI 316L at 300K: Back stress and effective stress. *Acta Mater* 47(13):3617–3632.
26. Zhu YT, Liao XZ, Wu XL (2012) Deformation twinning in nanocrystalline materials. *Prog Mater Sci* 57(1):1–62.
27. Ashby MF (1970) Deformation of plastically non-homogeneous materials. *Philos Mag* 21(170):399–411.
28. Gao HJ, Huang YG, Nix WD, Hutchinson JW (1999) Mechanism-based strain gradient plasticity - I. Theory. *J Mech Phys Solids* 47(6):1239–1263.
29. Gao HJ, Huang YG (2003) Geometrically necessary dislocation and size-dependent plasticity. *Scr Mater* 48(2):113–118.
30. Wu XL, et al. (2014) Synergetic strengthening by gradient structure. *Mater Res Lett* 2(4):185–191.
31. Zandrahimi M, et al. (1989) Effects of changes in strain path on work-hardening in cubic metals. *Metall Trans A* 20(11):2471–2482.
32. Tanaka K, Mori T (1970) The hardening of crystals by non-deforming particles and fibres. *Acta Metall* 18(8):931–941.

Supporting Information

Wu et al. 10.1073/pnas.1517193112

Calculation of True Plastic Strain for Elongated Grains

Assume that after tensile testing, an equiaxed grain of initial size l_0 elongates to an aspect ratio of $\alpha = l/w$, where l and w are the grain length and width, respectively.

During the plastic deformation, the volume is conserved, i.e.,

$$l_0^3 = lw^2 = l^3/\alpha^2. \quad \text{[S1]}$$

Then, the grain length l after tensile testing can be expressed as

$$l = l_0\sqrt[3]{\alpha^2}. \quad \text{[S2]}$$

The true plastic strain of the grain can be calculated as

$$\varepsilon = \ln\left(\frac{l}{l_0}\right) = \frac{2}{3}\ln\alpha. \quad \text{[S3]}$$